Photoacoustics 10 (2018) 20–30

Contents lists available at ScienceDirect

Photoacoustics

journal homepage: www.elsevier.com/locate/pacs

Research article

# Rapid scanning wide-field clutter elimination in epi-optoacoustic imaging using comb LOVIT

Tigran Petrosyan[a], Maria Theodorou[b], Jeff Bamber[b], Martin Frenz[a,*], Michael Jaeger[a]

[a] Institute of Applied Physics, University of Bern, Sidlerstrasse 5, 3012, Bern, Switzerland
[b] Joint Department of Physics and CRUK-EPSRC Cancer Imaging Centre, Institute of Cancer Research, and Royal Marsden NHS Foundation Trust, Downs Road, Sutton, Surrey, SM2 5PT, UK

ARTICLE INFO

*Article history:*
Received 14 September 2017
Received in revised form 22 December 2017
Accepted 13 February 2018
Available online 19 February 2018

*Keywords:*
Photoacoustic
Imaging depth
Handheld
Ultrasound
Radiation force
Shear wave
Image contrast

ABSTRACT

Epi-style optoacoustic (OA) imaging provides flexibility by integrating the irradiation optics and ultrasound receiver, yet clutter generated by optical absorption near the probe obscures deep OA sources. Localised vibration tagging (LOVIT) retrieves OA signal from images that are acquired with and without a preceding ultrasonic pushing beam: Radiation force leads to a phase shift of signals coming from the focal area resulting in their visibility in a difference image, whereas clutter from outside the pushing beam is eliminated. Disadvantages of a single-focus approach are residual clutter from inside the pushing beam above the focus, and time-intensive scanning of the focus to retrieve a large field-of-view. To speed up acquisition, we propose to create multiple foci in parallel, forming comb-shaped ARF patterns. By subtracting OA images obtained with interleaved combs, this technique moreover results in greatly improved clutter reduction in phantoms mimicking optical, acoustic and elastic properties of breast tissue.



## 1. Introduction

Optoacoustic (OA) or equivalently named photoacoustic (PA) imaging shows optical absorption contrast inside tissue with ultrasound spatial resolution, based on detection of thermoelastic ultrasound that is generated upon optical absorption when irradiating the tissue with pulsed laser light. An image can be reconstructed by time-resolved detection of these ultrasound signals. The basic mechanisms of OA imaging and underlying signal processing are thoroughly described in review articles [1–3].

OA imaging provides functional information via the display of the blood oxygen saturation level based on the difference in absorption spectra of oxy- and deoxyhemoglobin [4–7]. Thus, it is a promising tool for diagnosis of vascular diseases and cancer [8,9], as well as for monitoring treatment response [10–12]. The combination of classical ultrasound (US) and OA imaging in one device has been demonstrated as a safe, real-time, multimodal imaging modality [13–17] with promise for clinical diagnosis [16]. For this combination, an epi-style setup is favored such that irradiation and detection is performed from the same side of the tissue. The optical components can then directly be integrated into the acoustic probe, e.g. as a diode-based miniaturized multi-wavelength laser source [18]. Such a combined setup allows flexible single handed probe guidance and accessibility to body parts otherwise not reachable in transmission mode due to bones, acoustically attenuating tissues or gas-containing hollow organs [19].

On the downside, the epi-style setup generates clutter signals which limit signal-to-background ratio and decrease the imaging depth to values substantially less than the several centimeters predicted by the electronic noise level, detector bandwidth and acoustic attenuation in the tissue [20]. Clutter is caused by strong OA transients that are generated by optical absorption at the tissue irradiation site in proximity to the detecting transducer [21], e.g. by melanin, blood capillaries or vascular lesions [22,23]. Detection of transients that propagate straight to the transducer from outside the imaging plane ('direct clutter') or detection of echoes when transients propagate into the tissue and are scattered by acoustic impedance fluctuations ('echo clutter' or 'reflection artefacts') generates artefactual background signals. These background signals can overlap in time and may then be confused with weaker optoacoustic signals from light absorbing structures deep inside the tissue strongly reducing the signal to clutter ratio. For particular aspects of anatomy or function, the signal to clutter ratio can be enhanced by employing OA contrast agents (e.g. [24–28]). This approach, however, increases the imaging depth for only those

* Corresponding author.
*E-mail address:* frenz@iap.unibe.ch (M. Frenz).

https://doi.org/10.1016/j.pacs.2018.02.001

aspects of anatomy or function to which the agent localizes, and it is invasive.

To generally increase imaging depth towards the noise limited value, various clutter reduction techniques have been proposed:

(1) Displacement compensated averaging (DCA) employs the clutter decorrelation that results from quasi-static tissue deformation when palpating the tissue with freehand probe motion [29–31]. This technique is inherently limited by the maximum achievable deformation, typically resulting in a maximum threefold clutter reduction factor [17,29].
(2) Photoacoustic-guided focused ultrasound (PAFUSion) uses ultrasound pulse-echo acquisitions to mimic OA signal reflection artefacts, which can then be subtracted from the OA image for clutter reduction [32–35]. When using linear array probes for detection, this method can only mimic echo clutter that is generated by OA transients that propagate entirely within the imaging plane. Thus PAFUSion is well suited in a situation where the tissue must be irradiated directly below the probe aperture, to remove the significant echo clutter that stems from the plane-like OA transients generated by the skin melanin layer.
(3) Spatial coherence weighted OA imaging [36,37] exploits the fact that clutter frequently arises from OA sources, or echo-producing structures, that cover a volume that is much larger than the focal volume associated with a given image pixel, and thus the transients that they produce have low spatial coherence when they reach the detector. This allows their removal by a channel-level spatial coherence filter, but not without some loss of information, particularly from distributed but genuine OA sources.
(4) With the goal of allowing efficient clutter elimination that is independent of the clutter or signal origin, localized vibration tagging (LOVIT) was developed [38]. A long-pulsed (few 100 microseconds) focused ultrasonic beam generates acoustic radiation force (ARF) that induces localized tissue displacement at its focus (henceforth called single-focus LOVIT). OA images are acquired, with and without localized displacement of optically absorbing structures produced by preceding ARF pushes. Subtraction of the images results in a LOVIT image that highlights true OA signal at the focal region where the displacement is largest. Clutter signals that occur in the same region of the reconstructed image originate – by definition – from outside the focus. As the displacement outside the focal region is comparably small or even zero, clutter signals are reduced in the subtracted images. In a proof-of-principle study, efficient clutter reduction was demonstrated using a separate US transducer for ARF generation [38]. Recently, the performance of single-focus LOVIT was successfully demonstrated in a clinically realistic setup where the same linear array probe was used for ARF generation and imaging [39].

Combinations of the above approaches may eventually prove to be beneficial. For the moment however, LOVIT appears to be particularly promising and presents considerable opportunities for further development.

In single-focus LOVIT, clutter reduction is achieved only at one focal region at a time. Such an approach has the disadvantage of long acquisition times for scanning the focus position through an image, or a region of interest (ROI) within an image, which may limit clinical applicability in terms of real-time feedback. In addition, single-focus LOVIT does not completely eliminate echo clutter. It leaves residual echo clutter (henceforth, residual clutter): even though the displacement is largest inside the focal region of the ARF beam, significant displacement is generated also above the focal region and scatterers located there produce residual clutter inside the focal region if the total acoustic path length from a strong OA source to a scatterer and then to the detector equals that from the focal depth to the detector.

To circumvent these two problems, we propose a novel modification of LOVIT where multiple horizontally aligned foci are created simultaneously, forming comb-shaped ARF patterns. With this approach, imaging a large ROI can be accelerated compared to single-focus LOVIT, by a factor equal to the number of foci created within the comb. In addition to allowing a faster scanning time, comb LOVIT demonstrates a substantial reduction of residual clutter. To show this improvement, we compare the comb LOVIT and single-focus LOVIT approaches in a phantom study. Since detection of breast cancer is one of the promising application areas of OA imaging [40,41], we have chosen to compare the methods using a phantom that mimics optical, acoustic and elastic properties of breast tissue and contains optically absorbing inclusions mimicking blood vessels to allow signal to clutter ratios to be studied at various depths.

## 2. Theory

The acoustic radiation force (ARF) $f\left[N{\cdot}cm^{-3}\right]$ generated inside attenuating media by a focused ultrasonic beam can be calculated by [42]:

$$f(r,t) = \frac{2\alpha I(r,t)}{c}, \tag{1}$$

where $\alpha\left[cm^{-1}\right]$ is the ultrasound amplitude attenuation coefficient, $I\left[W{\cdot}cm^{-2}\right]$ the local intensity of the ultrasonic beam and $c$ the speed of sound. ARF accelerates the tissue along the ARF beam axis, which results in localized axial tissue displacement relative to the state that existed at the time before ARF beam transmission, turning into shear waves that propagate mainly in the lateral and elevational directions perpendicular to the beam axis. Shear wave speed is related to the Young's modulus $E$ of tissue in which the elastic modulus is orders of magnitude higher than the shear modulus via [43]:

$$c_s = \sqrt{\frac{E}{3\rho}}, \tag{2}$$

where $\rho$ is the density of the tissue. When irradiating with a limited ARF push duration of few hundred microseconds, and with shear wave speeds typically a few m/s in soft tissues, shear waves can propagate only few millimetres before the push ends. As a result, the axial tissue displacement after the end of the push shows a spatial profile as indicated in Fig. 1a. At the ARF beam focus, it is characterized by a narrow region of maximum displacement (henceforth, 'focal region'), which is broadened relative to the ARF focus diameter due to shear wave propagation but still contained within few millimetres diameter. A significant displacement is also found above and below the focal region, albeit rapidly decreasing along the intensity profile of the pushing beam.

The goal of LOVIT is to differentiate between clutter and true OA signals and ultimately, eliminate clutter. In single-focus LOVIT, a first OA image is acquired without preceding ARF push (no displacement is present at the time of OA acquisition), and a second one at a short delay after an ARF push (a sketch of the scan protocol is shown in Fig. 1b). The subtraction of the two images results in a LOVIT image. The axial displacement of optical absorbers by the ARF beam leads to an OA signal phase shift between the two acquisitions and thus a non-vanishing signal from these absorbers in the subtraction (LOVIT) image. The signal amplitude in the LOVIT image is thus determined by the ARF-induced displacement that occurs in the interval between the two OA acquisitions. For displacements that are substantially below

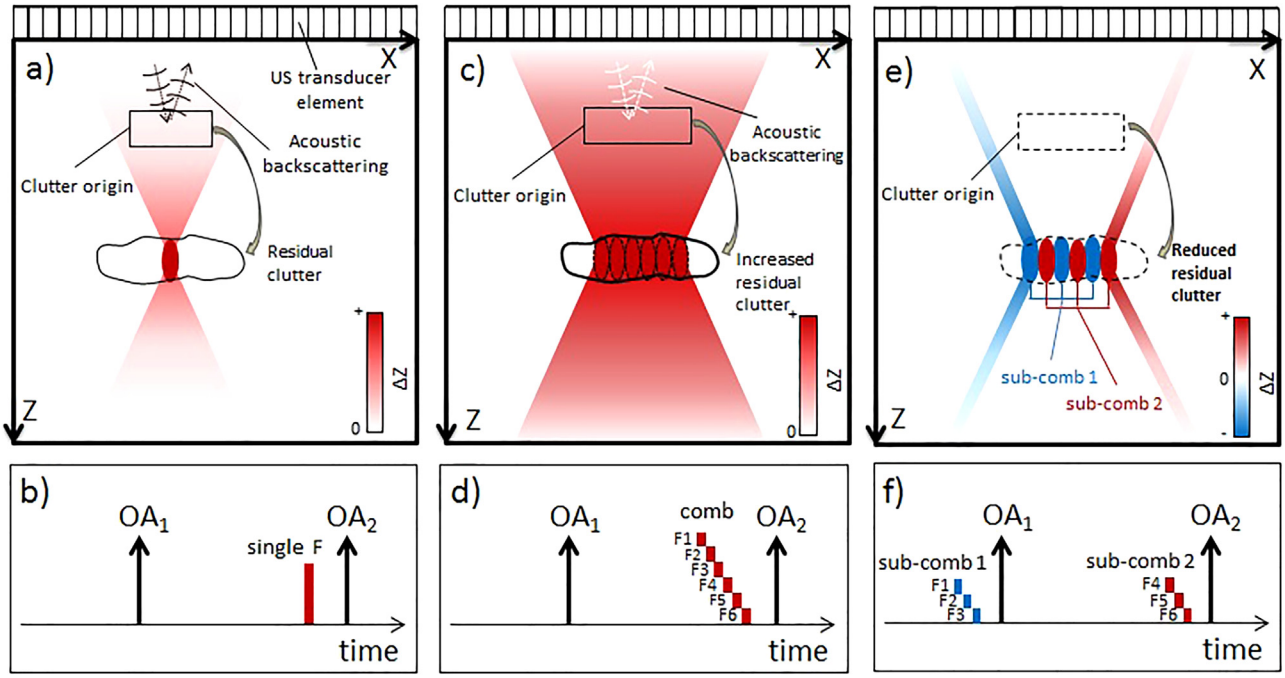


**Fig. 1.** (a) Sketch of the effective displacement profile in single-focus LOVIT. (b) Scan timing of single-focus LOVIT. A single-focus ARF transmission precedes one of two successive OA acquisitions. (c) Sketch of the summed effective displacement profile produced by multiple ARF foci (F1-F6) generated in parallel (the comb). (d) Scan timing when the full comb is generated before one of two OA acquisitions. (e) Sketch of the effective displacement between two interleaved sub-combs, illustrating the substantially reduced effective displacement at half the focal depth compared to (a) and (c). (f) Scan timing when alternating sub-combs are generated, a different sub-comb before each alternate OA acquisition.

half the acoustic wavelength $\lambda$ at the centre frequency of the probe, the LOVIT signal amplitude $S_L(x,z)$ at coordinates ($x$ = lateral, $z$ = axial) in the reconstructed image is linearly related to the product of the axial displacement $\Delta z(x,z)$ inside the imaging plane and the true OA signal amplitude $S(x,z)$ [38]:

$$S_L(x,z) \cong S(x,z)\cdot\Delta z(x,z)\cdot\frac{2\pi}{\lambda}, \tag{3}$$

Here and henceforth, $\Delta z$ is referred to as the displacement generated between any two OA acquisitions and will be termed effective displacement. In single-focus LOVIT, we assume that the tissue is in a mechanical equilibrium at the time of the OA acquisition without preceding ARF push. The effective displacement is thus identical to the displacement after the ARF push relative to this equilibrium state (henceforth, absolute displacement). Since the effective displacement is largest at the focal region, single-focus LOVIT highlights the true OA signals from inside the focal region according to Eq. (3). In order to highlight true OA signals inside a larger field of view, the focal region has to be scanned through the imaging plane.

Direct clutter that is generated by optically absorbing or echogenic tissue located outside the ARF beam, where no effective displacement occurs, shows no phase shift between the two acquisitions and is therefore fully eliminated by subtraction. However, when OA transients are backscattered from echogenic tissue above the focal region, the resulting echo clutter is not cancelled by subtraction: The effective displacement of ultrasound scatterers – even though smaller than at the focal region – results in a significant phase shift of the echoes. The resulting residual clutter appears inside the focal region of the reconstructed OA image when the round-trip travel distance from the OA source to the scatterers and back to the probe matches the focal depth. In the following we assume – for didactic purpose and without loss of generality – that residual clutter originates from acoustic scatterers located at exactly half the focal depth, which is mainly the case for epi-OA imaging where the main sources of strong OA transients are the skin melanin and skin vasculature. The amplitude of residual clutter $C_L(x_f,z_f)$ at the focal depth after subtraction can therefore be approximated analogous to Eq. (3) by a product:

$$C_L(x_f,z_f) \cong C(x_f,z_f)\cdot 2\cdot\Delta z\left(x_f,\frac{z_f}{2}\right)\cdot\frac{2\pi}{\lambda}, \tag{4}$$

where $C(x_f,z_f)$ is the amplitude of echo clutter signals that originate from backscattering at $\frac{z_f}{2}$ but are reconstructed at the focal depth $z_f$. $\Delta z\left(x_f,\frac{z_f}{2}\right)$ is the effective displacement of the scatterers located at half the focal depth. The factor two in Eq. (4) accounts for the fact that reconstructed echo clutter signals experience an apparent shift that is determined by the change in round-trip distance of echoes, up to twice the effective displacement of the scatterers. Note that this factor is accurate only when the clutter-producing OA transients propagate in the direction of the beam axis. An oblique propagation direction would result in a smaller increase in round-trip distance, and could be accounted for via a cosine law. For didactic simplicity of Eq. (4), however, this influence is neglected.

For optimal clutter reduction performance of LOVIT, two conditions must be fulfilled. First, to maximize amplitude and thus signal-to-noise ratio (SNR) of true LOVIT signals, the effective displacement inside the focal region should be as close as possible to half the acoustic wavelength $\lambda$ at the centre frequency of the transducer (e.g. 150 μm for a 5 MHz probe). Limited by ultrasound safety considerations, displacement magnitudes that are used *in vivo* in acoustic radiation force impulse (ARFI) imaging have been reported in the range of 5–40 μm, with ARF transmission periods between 100 and 500 μs [43–46]. For such effective displacement magnitudes, the linear approximation in Eq. (3) is valid. Second, to minimize residual clutter inside the focal region, the effective displacement at the location of the clutter-producing scatterer

should be as small as possible. To achieve efficient clutter reduction, the goal is therefore to maximise the ratio between $S_L$ and $C_L$, equivalent to minimising the ratio between the effective displacement at half the focal depth and at the focus.

As mentioned in the introduction, single-focus LOVIT has two limitations: (a) frame rate for clutter reduced imaging is limited by the need to scan the ARF focus sequentially throughout the imaged region, and (b) clutter reduction performance is limited by the existence of residual clutter.

Comb LOVIT addresses the issue of long acquisition times in single-focus LOVIT: Instead of scanning a single ARF focus, multiple ARF foci are created in parallel forming horizontal combs with focus positions separated by a uniform pitch as shown in the sketch in Fig. 1c (6 foci are depicted for demonstration). This can be achieved by modifying the single focus scan sequence: Instead of irradiating into a single focus position at a time, the ARF beam is steered in a quick succession to each focus position before acquiring the second OA frame as indicated in the scan protocol in Fig. 1d. At the given laser pulse repetition rate, this leads to a reduction of total acquisition time compared to single-focus LOVIT, by a factor equal to the number of foci within the comb. Acquiring, however, a pair of OA frames, one without and one with a preceding ARF comb (see Fig. 1d) has an important drawback: the combined effective displacement generated by the overlapping beams above the focal depth is larger than that when only a single ARF focus is generated (compare Fig. 1a and c). Therefore subtraction of pre- and post-ARF OA frames results in even stronger residual clutter than in the single-focus LOVIT approach.

To circumvent this problem, we developed a modified comb LOVIT in which the total number of foci inside a comb is split into two interleaved sub-combs (in our example $2 \times 3$ foci). The two sub-combs have double the original pitch and are shifted relative to each other in x-direction by one original pitch as shown in Fig. 1e. The two successive OA frames are acquired each preceded by one of the sub-combs (see scan sequence in Fig. 1f). When each OA acquisition is preceded by one of the two sub-combs, which alternate for alternating OA acquisitions, it is the effective displacement of clutter-producing scatterers between the two sub-combs – rather than the absolute displacement produced by each sub-comb – that determines the residual clutter level. By generating sub-combs with a smooth lateral profile of displacement magnitude at half the focal depth, the effective displacement in comb LOVIT can be much smaller than the absolute displacement in single-focus LOVIT. This is illustrated in Fig. 1e where the effective displacement at half the focal depth is zero in the region where the two sub-combs overlap. Only towards the lateral edges of the displacement profiles of the ARF beams that produce the two sub-combs, does a non-zero effective displacement exist, but overall this will result in substantially reduced residual clutter in comb LOVIT compared to single-focus LOVIT.

## 3. Materials and methods

### 3.1. Phantom

A tissue mimicking phantom was produced from 5% w/w gelatine in water. To mimic acoustic echogenicity and optical attenuation of human tissue, cellulose (4% w/w) was added to the bulk medium. To mimic blood vessels, the phantom additionally contained optically absorbing cylindrical inclusions (diameter 2 mm), made from the same 5% gelatine solution mixed with India ink (black, Winsor & Newton) and positioned at various depths with 5 mm axial intervals as shown in Fig. 2a. Only 0.4% w/w cellulose (ten times less than in the bulk) was used in the cylindrical inclusions to make them visible as hypoechoic regions in echo US similar to real blood vessels (see Fig. 2b). A more detailed description of the phantom production is given in reference [38]. The ARF beam transmissions tended to heat the surface of the transducer to up to 31 °C. Because the melting point of the gelatin was 23 °C, direct contact of the transducer to the phantom resulted in partial melting of the phantom surface. This was avoided by placing an optically transparent and acoustically matched polyacrylamide spacer of 5 mm thickness between the phantom and the transducer.

The performance of LOVIT is determined by the interplay between different tissue properties, as follows: The optical absorption coefficient of blood vessels determines their SNR in OA and LOVIT images, while the bulk effective optical attenuation coefficient determines the depth-dependent fluence distribution. The shear wave speed and the ultrasound attenuation coefficient in the phantom dictate the spatial distribution and the magnitude of the absolute displacement at the time of the OA acquisition, and

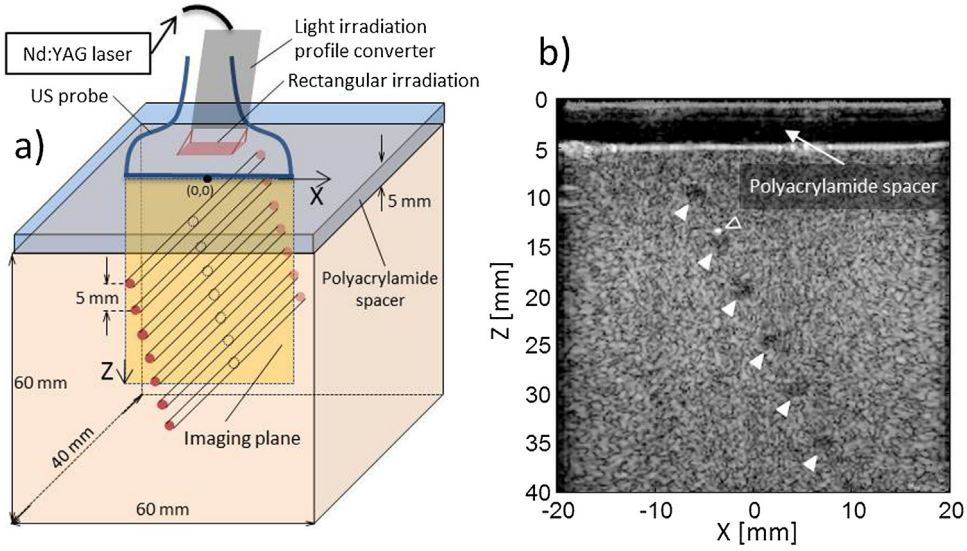


**Fig. 2.** (a) Sketch of the setup. The gelatine phantom contained cylindrical inclusions mimicking blood vessels, placed at various depths. The orientation of the US probe and the irradiation optics are indicated. The yellow rectangle visualizes the imaging plane of the US system. (b) B-mode US image of the phantom, showing the hypoechoic inclusions (full white arrows) and polyacrylamide layer on top. A small air bubble is noticed on top of the second inclusion (hollow white arrow).

the echogenicity of the background material determines the level of echo clutter.

To evaluate LOVIT in a realistic scenario, the phantom properties were chosen with the goal of mimicking a situation where blood vessels inside breast tissue are imaged by virtue of their absorption of near-infrared light. The 1064 nm wavelength that was employed in OA imaging (described below) was intended to serve as a surrogate for a broader wavelength range between 700 and 850 nm, i.e. the optical properties of the phantom at 1064 nm were chosen to represent tissue optical properties in this range. The absorption coefficient of the ink solution for the cylindrical inclusions ($\mu_a = 5\ \mathrm{cm}^{-1}$) was measured using an optical spectrometer (LAMBDA 750, Perkin Elmer Inc, MA, USA) and mimics the absorption coefficient of blood at 800 nm. The effective attenuation coefficient of the background medium was measured to be $0.9 \pm 0.15\ \mathrm{cm}^{-1}$ at 1064 nm, based on the depth dependent amplitude of the OA signal of the absorbing inclusions. This value was within the $0.8\ \mathrm{cm}^{-1}$ to $1.1\ \mathrm{cm}^{-1}$ reported for breast tissue in the wavelength range between 675 and 850 nm [47,48]. The technique for estimating the shear wave speed in the background medium was inspired by shear wave elastography [43,49]: After transmitting an ARF burst, focused at (x = 0, z = 20 mm) location, a sequence of US frames were acquired at ultrafast rate. From these US frames the displacement profile as a function of time was quantified via echo phase correlation. The estimated shear wave speed, $1 \pm 0.05$ m/s was within the 0.9 to 1.2 m/s range reported for uncompressed breast tissue [50]. According to Eq. (2), this corresponds to a Young's modulus of 3 kPa that is typical for breast [51]. The shear wave speed was repeatedly monitored between different experiments to assure the stability of the phantom in terms of its elastic properties. The speed of sound in the phantom's background material was measured using US time-of-flight through separate samples prepared from the same mixture, and found to be $1515 \pm 20$ m/s, which corresponds to reference values of human glandular breast tissues (~1530 m/s [52]). Optical absorption inside the bulk medium below the irradiated surface was sufficiently strong – in combination with the chosen density of ultrasonically scattering cellulose – to produce echo clutter on a level that is – in our experience – representative for handheld epi- OA imaging in the wavelength range from 700 to 1064 nm.

### 3.2. Setup

A sketch of the setup is shown in Fig. 2a. Combined OA and US imaging was implemented on a Verasonics research ultrasound system (Vantage 64 LE, Verasonics Inc., Redmond WA, USA), combined with a 128 element, 0.3 mm element pitch, 5 MHz centre frequency and 3 MHz bandwidth linear array probe (ATL L7-4, Philips, NL). The system allows individual programming of the transmit-pulse timing for each element and parallel acquisition of received signals on 64 elements. For OA signal generation a Q-switched Nd-YAG laser with a wavelength of 1064 nm, a pulse length of 6 ns and a repetition rate of 10 Hz was used (BrilliantB, Quantel, Les Ulis, F). The laser light was guided through an optic fibre bundle ending in a rectangular area that irradiated the phantom surface alongside the probe aperture through a $7 \times 20\ \mathrm{mm}^2$ rectangular profile. The total pulse energy at the output of the fibre bundle was 130 mJ, resulting in $93\ \mathrm{mJ/cm}^2$ radiant exposure, a value just below the ANSI limit at 1064 nm. At 800 nm, the ANSI limit is substantially lower, i.e. $32\ \mathrm{mJ/cm}^2$. Within that safety limit, the same SNR can be achieved by irradiating on both sides of the probe like in [29], and by additionally enlarging the irradiation areas.

The same linear array probe was used for generating the focused ARF beams, by driving the transducer elements with a sinusoidal pulse at the probe's centre frequency of 5 MHz. Focusing was achieved by applying appropriate transmit phases to the individual transducer elements. As far as possible, the number of elements used for ARF beam focusing was adjusted to achieve an angular aperture of 60°, limited by an angle range from −30° to +30°. The angle limits were determined by the element pitch (0.3 mm), which was identical to the acoustic wavelength at the centre frequency of the probe and resulted in disturbing grating lobes above these limits. Smaller aperture angles were not desired because they result in axial elongation of the displacement profile and thus in a higher ratio of effective displacements between half the focal depth and the focus and, hence, increased residual clutter.

### 3.3. Acquisition protocol

To enable a one-to-one comparison in terms of clutter reduction efficiency between comb LOVIT and single-focus LOVIT, care was taken that acquisition parameters were chosen as close as possible between the two techniques.

For the single-focus LOVIT, the ARF focus was scanned inside a region of interest (ROI) of the phantom with a step size of 1.25 mm in lateral (x) and 5 mm in axial (z) direction, from z = 9 mm to 29 mm resulting in 5 scanning depths (z = 0 defined as the surface of the probe array), and from x = −6.9 mm to 6.9 mm resulting in 12 positions (x = 0 defined as the centre of the probe aperture). The scanning step size for each direction was chosen to be comparable to the respective FWHM of the displacement distribution at the focus. The timeline of the data acquisition is shown in Fig. 3a. For each focus position, a set of OA acquisitions – composed of one OA frame without ("pre-ARF) and one with ('post-ARF') preceding ARF pulse– was repeated 20 times for averaging. In LOVIT, residual reverberations of the ARF ultrasound power inside the phantom or tissue can cause additional noise at the time of OA acquisition. In the attempt to minimize such reverberations while maintaining an as narrow as possible focal region, the OA acquisition was performed with a post-ARF delay of 0.8 ms after the end of the ARF pulse. The 20 sets of OA acquisitions were followed by an acquisition of an US frame without and one with preceding ARF pulse using the same post-ARF delay. The US images where used to quantify the magnitude of the effective displacement between OA acquisitions via echo phase correlation of the pre- and the post-ARF US images. A composite LOVIT image of the ROI was generated by mosaicking the LOVIT results of all focal regions.

For a one-to-one comparison, we aimed to achieve similar displacement magnitudes at the foci in comb LOVIT compared to single-focus LOVIT. One way to implement comb LOVIT would be to distribute the total 12 lateral focus positions on one group of two interleaved sub-combs each with 6 focus positions at a 2.5 mm pitch per sub-comb. This has, however, a disadvantage: The lateral profile of the effective displacement between two sub-combs has zero crossings at half way between adjacent focus positions, which would lead to regions of missing data at these locations in the final LOVIT image. This problem can be solved when distributing the total 12 lateral focus positions on two combs with 6 focus positions, each comb built from two interleaved sub-combs with 3 foci at a 5 mm pitch. The first comb contains two interleaved sub-combs covering the uneven focus numbers, the second comb covers the even focus numbers. In that way, the two combs complement each other's zero crossings, enabling the generation of a final LOVIT image without missing data regions.

When steering the ARF beam focus sequentially to each focus position, different focus positions are insonified at different times so that shear waves propagate different distances between ARF generation and OA acquisition. The shear wave propagation would thus result in different displacement magnitudes and profiles for different foci. To avoid this problem, the duration of the ARF push

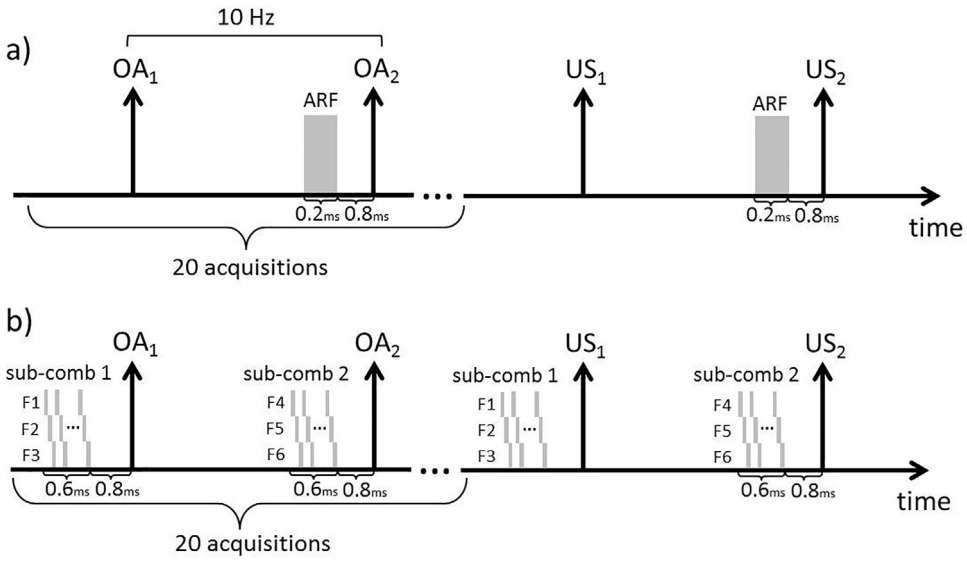


**Fig. 3.** Data acquisition timeline with (a) single-focus LOVIT for one focus position, and (b) comb LOVIT for one comb. F1, F2, F3 correspond to the foci created by the first sub-comb, and F4, F5, F6 to the second sub-comb. Two groups of two interleaved sub-combs were used to cover the total 12 lateral focus positions.

per focus was split into a number of active intervals that were interleaved between different foci in time to achieve a quasi-simultaneous transmission into all focus positions (time-multiplexing) as illustrated in Fig. 3b. As a consequence, the total pulse duration per focus position in the comb LOVIT was 0.6 ms (but only 0.2 ms out of these were active), whereas it was 0.2 ms with the single-focus LOVIT.

For each pair of interleaved sub-combs, a set of two OA acquisitions following the first and second sub-comb was repeated 20 times for averaging as indicated in Fig. 3b. As with single-focus LOVIT, the same sequence was repeated with US acquisitions, for quantifying the effective displacement between sub-combs. In order to simultaneously display the clutter-reduced OA signal from all focal positions in the full scanned ROI, a composite LOVIT image was generated by mosaicking the LOVIT results from the focal regions of the different combs.

## 4. Results

Fig. 4a shows the conventional OA image, where significant clutter is noticed starting from around 10 mm depth, limiting contrast and imaging depth. The 10 mm depth correspond to the elevational offset between the rectangular laser irradiation profile and the imaging plane which determines the first arrival of clutter signals [23]. Only the top and bottom edge of the absorbing inclusions are visible due to the limited bandwidth and limited receive aperture of the transducer [53,54]. The composite LOVIT images obtained by single-focus LOVIT and comb LOVIT are shown in Fig. 4b and 4c respectively, where the ROI that was covered with the ARF foci is indicated by a solid rectangle. For display, the envelope was logarithmically compressed to a range of 40 dB. To allow a fair visual comparison of contrast, the offset of the dB range was adjusted in each image so that the inclusion at 19 mm depth is shown with an identical gray level.

Both LOVIT methods demonstrate a substantial clutter reduction and improved contrast compared to the conventional OA image. The inclusion at 19 mm depth in the conventional OA image is hard to see without *a priori* knowledge of its location, and yet it can be clearly identified in the LOVIT images. The inclusion at 24 mm depth, which is not visible in the conventional OA image, can be clearly identified in the LOVIT images. The bottom edge of that inclusion is not identified in the single-focus LOVIT image without *a priori* knowledge of its location since its intensity level blends in with the surrounding residual clutter. With comb LOVIT this inclusion can yet be clearly distinguished from the background due to substantial reduction of residual clutter (Fig. 4c). A strong reflection artefact is visible at 26–28 mm depth indicated by a solid ellipse in the single-focus LOVIT image (Fig. 4b). This artefact is residual echo clutter originating from the air bubble at 13 mm depth (see Fig. 2b). Its prominent intensity compared to the

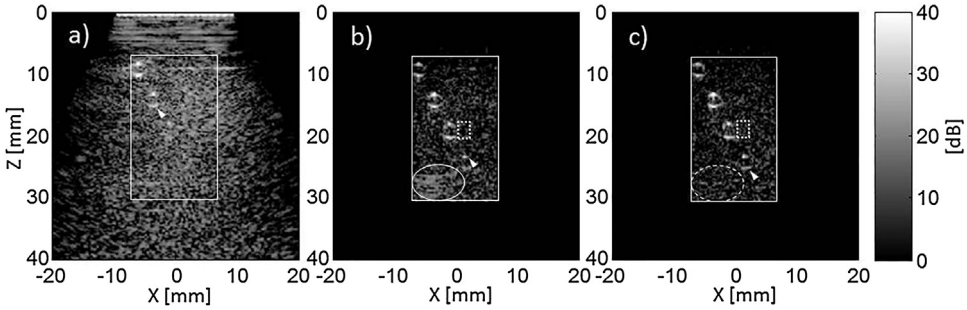


**Fig. 4.** (a) Conventional OA image. (b) Composite LOVIT image obtained by mosaicking in scanning single-focus LOVIT. (c) Composite LOVIT image obtained by mosaicking multiple combs in comb LOVIT. In (b) and (c) the solid rectangle shows the ROI scanned with ARF foci. In all the images, white arrows indicate the deepest visible OA signal. A strong reflection artefact indicated by an ellipse in (b), is substantially reduced in (c). The area inside the dotted rectangle in (b) and (c) was used to quantify the background level.

average residual clutter is due to the compression of the air bubble in the ARF beam, which locally led to a larger displacement around the air bubble compared to the surrounding medium. We intentionally kept this result, as it illustrates the advantage of comb LOVIT over single-focus LOVIT in eliminating echo clutter: This artefact cannot be distinguished from the background in Fig. 4c, indicating that the residual clutter that was still visible in Fig. 4b was reduced to below the noise level in Fig. 4c.

Fig. 5 shows the US-measured ARF induced spatial distribution of the effective displacement in single-focus LOVIT and comb LOVIT for 19 mm (a, c) and 29 mm (b, d) focal depths. Only one comb consisting of two interleaved sub-combs is shown per depth. For a more quantitative comparison, axial profiles of the effective displacement were taken at the lateral center of each focus position and averaged over all foci per comb (Fig. 5e and f for the two focal depths). The achieved peak displacements of $32 \pm 3$ μm at 19 mm focal depth, and $24 \pm 3$ μm at 29 mm focal depth were within the range of what has been achieved *in vivo* in ARFI imaging. Fig. 5e and f demonstrate how the effective displacement profile extends above and below the focal depth in single-focus LOVIT. In comb LOVIT, the effective displacement above the foci – in particular also at half the focal depth – is substantially smaller than with single-focus LOVIT.

The total pulse duration in comb LOVIT was 0.6 ms (but only 0.2 ms of this period was used for active transmission), whereas it was 0.2 ms with the single-focus LOVIT. Even though shear wave propagation begins during the ARF push, the different total pulse durations had a negligible influence on the results in Fig. 5: This is expected because the magnitude and diameter of the displacement regions are mainly determined by the effective average time of shear wave propagation, i.e. the delay between the center of the ARF push duration and image acquisition. This value was similar between the two LOVIT approaches, i.e. 0.9 ms for single-focus LOVIT and 1.1 ms for comb LOVIT.

To quantify the clutter reduction performance of LOVIT, first we concentrate on the inclusion at 19 mm depth. This inclusion is at the limit of detectability in the conventional image, but allows an identification of contrast for comparison to LOVIT results. In order to quantitatively assess the contrast improvement of this inclusion, the signal-to-background ratio (SBR) was determined. The signal was defined as the maximum squared amplitude of the inclusion signal, and the background level was defined as the mean square amplitude in the dotted rectangular regions to the right side of that inclusion as indicated in Fig. 4b and c. For comparison, the noise level was also quantified, based on data that was acquired using the same acquisition protocols as for the conventional OA and LOVIT results but without laser radiation. We explicitly included ARF beam transmission when determining the LOVIT noise level, because residual reverberations of ARF ultrasound power at the time of OA acquisition can contribute to the noise in LOVIT.

The results of this analysis are summarized in Table 1. A substantial increase in SBR is demonstrated with single-focus LOVIT ($14.6 \pm 0.6$ dB) and comb LOVIT ($16.1 \pm 0.6$ dB) techniques compared to conventional OA imaging. Comb LOVIT shows a slightly higher SBR than the single-focus LOVIT in agreement with what was observed in the images in Fig. 4. The higher noise level of LOVIT compared to conventional OA imaging can be explained by residual reverberations of ARF ultrasound power at the time of OA acquisition. A slightly higher noise level is observed for comb than for single-focus LOVIT, but within the standard error of the noise measurements. Even for the inclusions at 9 and 14 mm depths, which were clearly visible even in the conventional image, a significant improvement in SBR by single-focus LOVIT (by $3.5 \pm 0.6$ dB and by $13.4 \pm 0.6$ dB, respectively) and by comb LOVIT (by $4.5 \pm 0.6$ dB and by $15.0 \pm 0.6$ dB, respectively) was observed compared to the conventional image.

As described in the Materials and Methods section, the number of active elements that could be used for ARF beam transmission depended on the ARF focus depth when keeping a constant angular aperture spanning from −30° to +30°. This led to different transmitted power depending on focus depth. Fig. 6 shows mosaics of the displacement maps as function of focus position with single-focus LOVIT and comb LOVIT. It can be seen that the displacement magnitude varied with focus depth and position. For the chosen phantom, the maximum displacement was reached at the depth of around 20 mm. For smaller depths, the decrease of

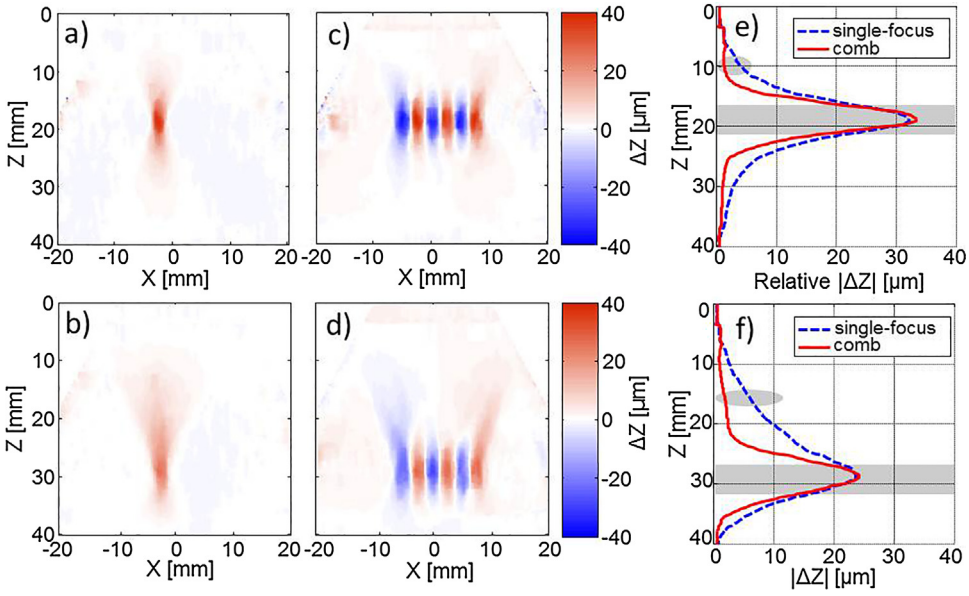


**Fig. 5.** (a-b) Effective displacement in single-focus LOVIT at (a) 19 mm and (b) 29 mm focal depths. (c-d) Effective displacement in comb-LOVIT at (c) 19 mm and (d) 29 mm focal depths. The foci with negative effective displacement in (c) and (d) correspond to the first sub-comb, the ones with positive effective displacement to the second sub-comb. Axial profiles of effective displacement through the center of the foci are shown in (e) and (f) for the corresponding focal depths. The grey rectangles in (e) and (f) indicate the 5 mm axial range around the focal depth that was used to construct the composite LOVIT image. The grey ellipses at around half the focal depth in (e) and (f) indicate the depth from where most residual echo clutter originates.

**Table 1**
Signal, background, noise levels and SBR for conventional OA, single-focus LOVIT and comb LOVIT for the absorbing inclusion at 19 mm depth. The dB scale is chosen relative to the noise level of the conventional image.

| | Signal level [dB] | Background level [dB] | SBR [dB] | Noise [dB] |
|---|---|---|---|---|
| Conventional OA | 38.7 | 28.2 ± 0.6 | 10.5 ± 0.6 | 0 ± 0.6 |
| Single-focus LOVIT | 30.9 | 5.8 ± 0.6 | 25.1 ± 0.6 | 2.8 ± 0.6 |
| Comb LOVIT | 30.8 | 4.2 ± 0.6 | 26.6 ± 0.6 | 3.3 ± 0.6 |

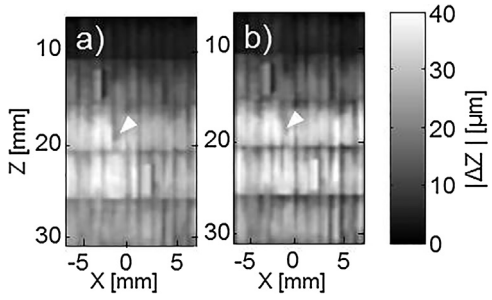


**Fig. 6.** Mosaicked displacement maps within the LOVIT ROI with (a) single-focus LOVIT and (b) comb LOVIT. The white arrows indicate the location of the inclusion at 19 mm depth where 25 μm local displacement was observed.

displacement magnitude is explained by the smaller number of active transducer elements resulting in reduced transmitted power, whereas for larger depths the decrease may be explained by ultrasound attenuation. The noticeable variations in the lateral direction may be explained by spatial variations of either shear elastic properties or ultrasound absorption or scattering. We would like to point out that – for identical focal positions – the displacement magnitudes varied within only 10% between the two LOVIT approaches.

## 5. Discussion

Contrast in conventional epi-OA images is limited by background that consists of a combination of clutter and system noise. In agreement with previous studies [38,39], significant clutter reduction and strongly improved contrast and imaging depth was demonstrated in the present results with single-focus LOVIT.

The primary goal of this study was to determine whether comb LOVIT could achieve at least the same contrast improvement as single-focus LOVIT, while enabling a faster scanning speed. Increasing scanning speed is necessary for real-time visual feedback, and is needed for clinical application of LOVIT-enabled clutter reduction. With the presented implementation the acquisition time was decreased by a factor of 6 compared to the single-focus LOVIT. This factor is determined by the total number of foci created within two sub-combs. With our 10 Hz laser system, it takes 2 s to acquire one composite comb LOVIT image with a ROI of $15 \times 25$ mm$^2$, which translates to a frame rate of 0.5 fps. This frame rate can, however, be further increased with increasing laser repetition rate $f$, up to the point $f_{max}$ where the pulse-to-pulse period $1/f_{max}$ equals the time it takes for the shear wave to propagate out of the chosen ROI. With a shear wave speed of 1 m/s and the chosen width of the ROI of 15 mm, $f_{max} \cong 66Hz$, allowing up to 3.3 fps frame rate in comb LOVIT.

In addition to reduced acquisition time, we demonstrate improved clutter reduction efficiency with comb LOVIT. In single-focus LOVIT, the residual clutter was still above the noise level. Using comb LOVIT the background signal was further reduced by 1.5 dB as shown in Table 1. The images in Fig. 4 were averaged over 20 acquisitions, which provided a sufficiently small noise level to clearly visualize the contrast improvement achieved with comb LOVIT compared to single-focus LOVIT. From those LOVIT images, however, it is not possible to conclude how small the residual clutter level was compared to the noise level. To answer this question, the average background level and the noise level were determined at the location without an inclusion at 19 mm depth as a function of the number of acquisitions averaged with single-focus and comb LOVIT using the same methodology as in Table 1. Fig. 7 shows these supplementary results on a linear scale. With increasing number of averages, the background level in the single-focus LOVIT converges to a constant level indicating the residual clutter. In comb LOVIT, the background level decreases far below the value that was obtained with 20 times averaging, indicating that the comb LOVIT image in Fig. 4c was actually limited by noise rather than by residual clutter. It is hard to conclude from Fig. 7 to which value the background level would eventually converge with further averaging. It is still possible, however, to roughly quantify the residual clutter level. Assuming that noise and residual clutter are uncorrelated, the expectation value of the total background level is the sum of the expectation values of noise and residual clutter level (all mean square). In the linear display of the mean square background level in Fig. 7, the residual clutter levels can therefore be estimated based on the difference between the background and noise level to 1.8 ± 0.3 for single-focus LOVIT and 0.15 ± 0.02 for comb LOVIT. This indicates a reduction of residual background by a factor of 12 ± 4.

The reduced level of residual clutter in comb LOVIT compared to single-focus LOVIT can be explained by the ratio between the displacement magnitudes at half the focal depth and at the focus position: the smaller this ratio, the more efficient the clutter reduction. We denote this ratio $R_{single} = \frac{\Delta z_{single}(z_f/2)}{\Delta z_{single}(z_f)}$ for single-focus LOVIT and $R_{comb} = \frac{\Delta z_{comb}(z_f/2)}{\Delta z_{comb}(z_f)}$ for comb LOVIT, where $z_f$ is the focal

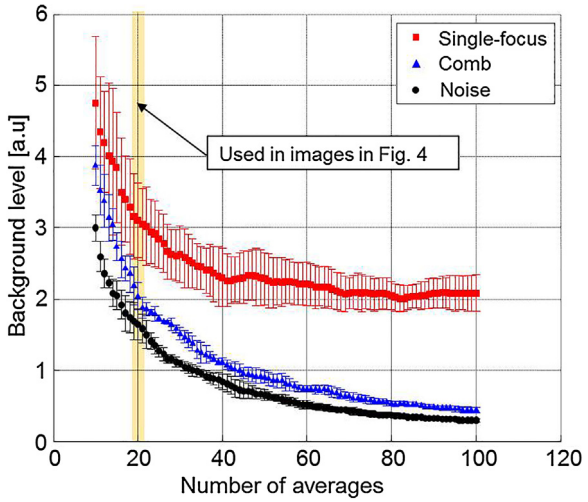


**Fig. 7.** Background levels (mean square amplitude) of single-focus LOVIT and comb LOVIT images averaged over the small analysis ROI at around 19 mm depth outside the inclusion (dotted rectangle in Fig. 4) compared to system noise level (comb ARF applied) for different numbers of acquisitions averaged. The errorbars indicate the standard deviation over three repetitions of the experiment.

depth. Since conservation of total power along the ARF beam axis dictates non-zero displacement at half the focal depth, residual clutter is inevitable in single-focus LOVIT where the effective displacement between two OA acquisitions is equal to the absolute displacement. In comparison, comb LOVIT is not limited by the displacement at half the focal depth, but by the effective displacement between two interleaved sub-combs, which can be substantially smaller. Table 2 shows the values of $R_{single}$ and $R_{comb}$ together with the effective displacement magnitudes at the focus and half the focal depth generated by single-focus LOVIT and comb LOVIT for 19 and 29 mm focal depths. $R_{comb}$ was reduced by a factor of $3.7 \pm 0.4$ compared to $R_{single}$ for 19 mm focal depth, which can explain a reduction in residual clutter level (mean squared amplitude) by a factor of $13.7 \pm 3.0$ with comb LOVIT, in agreement with what was observed in Fig. 7.

$R_{single}$ and $R_{comb}$ increase with increasing focal depth due to ultrasound attenuation: The longer the ARF beam path, the more acoustic energy is absorbed, resulting in less power reaching the focus relative to half the focal depth. Table 2 shows that the effective displacement at the focal region decreased from $32 \pm 3$ (single-focus) and $33 \pm 3$ μm (comb) to $24 \pm 3$ μm (single-focus and comb) when increasing the focal depth from 19 to 29 mm. At the same time, the effective displacement at half the focal depth was increased from $3.5 \pm 0.1$ to $5.1 \pm 0.1$ μm (single-focus) and from $1.0 \pm 0.05$ to $1.2 \pm 0.05$ μm (comb). This led to an increase in $R_{single}$ by a factor of $2 \pm 0.2$ and $R_{comb}$ by a factor of $1.7 \pm 0.2$. As a result, the ratio between $R_{comb}$ and $R_{single}$ was roughly the same for both focal depths. For the inclusion at 24 mm depth (deepest visible inclusion in both LOVIT images), SBR was improved by $1.4 \pm 0.6$ dB with comb LOVIT compared to single-focus LOVIT, which is similar to the improvement obtained for the inclusion at 19 mm depth (see Table 1). In other words, comb LOVIT outperforms single-focus LOVIT independent of depth.

As indicated earlier on, ultrasound attenuation is an important tissue parameter determining LOVIT SNR (via effective displacement inside the focal region) and clutter reduction efficiency (via $R_{single}$ or $R_{comb}$). The acoustic attenuation coefficient was determined based on the displacement magnitudes at the focus at 19 and 29 mm focal depths, taking into account that the decrease in displacement magnitude with increasing focal depth is determined by the interplay of ultrasound attenuation and the number of transmitting elements. The resulting value of $\alpha$ of $3.4 \pm 0.6 dB/cm$ compares well to an $\alpha$ of $3.6 \pm 1.1 dB/cm$ at 5 MHz that was reported in breast fat [55]. The effect of the US attenuation may be more important for tissues with higher $\alpha$, such as muscle for which an $\alpha$ of $5.5 \pm 0.5 dB/cm$ at 5 MHz was reported [56]. The higher the acoustic attenuation coefficient $\alpha$, the more acoustic energy is absorbed before reaching the focus, resulting in less power in the focus relative to half the focal depth. This leads to an increase in $\Delta z_{single}(z_f/2)$ and decrease in $\Delta z_{single}(z_f)$, and hence, increase in $R_{single}$. With increasing $\alpha$, single-focus LOVIT will quickly approach to $R_{single} = 0.5$, a breaking point where – according to Eq. (3) and (4) – the ratio between residual clutter $C_L$ and true LOVIT signal amplitude $S_L$ is equal to the original ratio between clutter $C$ and signal $S$ and hence no clutter reduction occurs. Since $R_{comb}$ is several factors smaller than $R_{single}$, comb LOVIT will allow clutter reduction in a broader range of $\alpha$.

Shear wave speed is another tissue parameter that influences the displacement distribution. Shear wave propagation during the ARF push and post-ARF delay broadens the diameter of the displacement region at the focus compared to the diameter of the ARF beam focus. The phantom in this study mimics breast tissue well in this respect, with a shear wave speed of 1 m/s ($E \sim 3kPa$). Other tissues have higher shear wave speeds, e.g., liver ~2 m/s ($E \sim 12kPa$) and muscle ~3 m/s ($E \sim 27kPa$) [57]. On one hand, a higher stiffness results in smaller displacement magnitudes at the focus hence reduction in SNR according to Eq. (3). On the other hand, a higher shear wave speed leads – for identical ARF push duration – to a broader focal displacement region in the lateral as well as the axial direction. This results in smaller displacement magnitudes at the focus compared to that at half the focal depth, which reduces SNR and clutter reduction efficiency. In addition, a high shear wave speed may limit the number of foci that can be used in comb LOVIT. Further research is thus required to optimize the trade-off between ARF push duration, the number of foci and the size of the ROI in comb LOVIT for different shear wave speeds. Such an optimization could take advantage by using the ability of shear wave elastography to pre-calibrate the tissue being imaged.

Various clutter reduction techniques are suited for different scenarios. PAFUSion demonstrated an average of 13 dB improvement in SBR *in vivo* at <10 mm depths in the proximity to superficial vasculature [33]. This technique has been shown to be efficient if clutter originates from reflections of OA transients that are generated at the skin surface directly below the US transducer. PAFUSion is thus mostly suited for superficial imaging when irradiation in the imaging plane is required, e.g., to achieve sufficient SNR with low laser pulse energies. With DCA, an improvement of 10 dB (around a factor of three in amplitude) in SBR was reported [29]. DCA also reduces clutter that arises from out-of-plane OA sources but is mainly suited for clutter reduction at depth where a sufficient displacement magnitude relative to the transducer can be achieved. Comb LOVIT demonstrated an improvement in SBR of 15 dB with 20 times averaging and a laser pulse energy around 100 mJ, parameters that allow a few cm imaging depth in real tissue. Limited by the transducer aperture, LOVIT is well suited for depths starting from ~10 mm. These are the depths where clutter usually becomes a significant limitation, when tissue is irradiated outside the imaging plane. Most importantly, comb LOVIT demonstrates elimination of all clutter types independent of location of origin.

**Table 2**
Ratios between the displacement magnitudes at half the focal depth and at the focus with single-focus LOVIT ($R_s$) and comb LOVIT ($R_c$) at 19 and 29 mm focal depths. The displacement values are averaged over all the focus positions used for each focal depth (errors in SD).

| | $f$ [mm] | $\Delta z(f)$ [μm] | $\Delta z(f/2)$ [μm] | $R_{single}$ or $R_{comb}$ |
|---|---|---|---|---|
| Single-focus LOVIT | 19 | $32 \pm 2$ | $3.5 \pm 0.1$ | $0.11 \pm 0.005$ |
| | 29 | $24 \pm 3$ | $5.1 \pm 0.1$ | $0.21 \pm 0.01$ |
| Comb LOVIT | 19 | $33 \pm 3$ | $1.0 \pm 0.05$ | $0.03 \pm 0.003$ |
| | 29 | $24 \pm 3$ | $1.2 \pm 0.05$ | $0.05 \pm 0.003$ |

## 6. Conclusion

This study indicates that, for breast tissue and tissues having similar properties, comb LOVIT holds promise for efficient clutter reduction in hand-held epi-OA imaging. In comparison to single-focus LOVIT, it allows an increase in acquisition speed by a factor equal to the number of foci in the comb, and considerably improved clutter reduction.

## Conflict of interest

The authors declare that there are no conflicts of interest.

## Acknowledgements

This research has received funding in part from the Swiss National Science Foundation (No. 205320_144443), from the European Union's Horizon 2020 research and innovation programme under grant agreement No 731771, Photonics Private

Public Partnership, and is supported by the Swiss State Secretariat for Education, Research and Innovation (SERI) under contract number 16.0160. We acknowledge support from the CRUK Centre for Cancer Imaging at the Institute of Cancer Research (grant number 1060/A16464) and from René Nyffenegger for his valuable contribution to the experimental work.

## References

[1] P. Beard, Biomedical photoacoustic imaging, Interface Focus 1 (4) (2011) 602–631.
[2] M. Xu, L.V. Wang, Photoacoustic imaging in biomedicine, Rev. Sci. Instrum. 77 (4) (2006) 041101.
[3] S. Manohar, D. Razansky, Photoacoustics: a historical review, Adv. Opt. Photonics 8 (4) (2016) 586–617.
[4] H.F. Zhang, K. Maslov, G. Stoica, L.H.V. Wang, Functional photoacoustic microscopy for high-resolution and noninvasive in vivo imaging, Nat. Biotechnol. 24 (7) (2006) 848–851.
[5] J. Laufer, D. Delpy, C. Elwell, P. Beard, Quantitative spatially resolved measurement of tissue chromophore concentrations using photoacoustic spectroscopy: application to the measurement of blood oxygenation and haemoglobin concentration, Phys. Med. Biol. 52 (1) (2007) 141–168.
[6] K.G. Held, M. Jaeger, J. Ricka, M. Frenz, H.G. Akarcay, Multiple irradiation sensing of the optical effective attenuation coefficient for spectral correction in handheld OA imaging, Photoacoustics 4 (2) (2016) 70–80.
[7] B. Cox, J.G. Laufer, S.R. Arridge, P.C. Beard, Quantitative spectroscopic photoacoustic imaging: a review, J. Biomed. Opt. 17 (6) (2012) 0612021–06120222.
[8] S.A. Ermilov, T. Khamapirad, A. Conjusteau, M.H. Leonard, R. Lacewell, K. Mehta, T. Miller, A.A. Oraevsky, Laser optoacoustic imaging system for detection of breast cancer, J. Biomed. Opt. 14 (2) (2009) 024007.
[9] D.R. Bauer, R. Olafsson, L.G. Montilla, R.S. Witte, 3-D photoacoustic and pulse echo imaging of prostate tumor progression in the mouse window chamber, J. Biomed. Opt. 16 (2) (2011) 026012.
[10] J. Yao, K.I. Maslov, Y. Zhang, Y. Xia, L.V. Wang, Label-free oxygen-metabolic photoacoustic microscopy in vivo, J. Biomed. Opt. 16 (7) (2011) 076003.
[11] J. Laufer, P. Johnson, E. Zhang, B. Treeby, B. Cox, B. Pedley, P. Beard, In vivo preclinical photoacoustic imaging of tumor vasculature development and therapy, J. Biomed. Opt. 17 (5) (2012) 0560161–0560168.
[12] S.Y. Nam, E. Chung, L.J. Suggs, S.Y. Emelianov, Combined ultrasound and photoacoustic imaging to noninvasively assess burn injury and selectively monitor a regenerative tissue-engineered construct, Tissue Eng. Part C, Methods 21 (6) (2015) 557–566.
[13] M.K.A. Singh, W. Steenbergen, S. Manohar, Handheld probe-based dual mode ultrasound/photoacoustics for biomedical imaging, Frontiers in Biophotonics for Translational Medicine, Springer, Singapore, 2016, pp. 209–247.
[14] J.J. Niederhauser, M. Jaeger, M. Frenz, Comparison of laser-induced and classical ultrasound, P Soc Photo-Opt Ins 4960 (2003) 118–123.
[15] J.J. Niederhauser, M. Jaeger, R. Lemor, P. Weber, M. Frenz, Combined ultrasound and optoacoustic system for real-time high-contrast vascular imaging in vivo, IEEE Trans. Med. Imaging 24 (4) (2005) 436–440.
[16] A. Aguirre, P. Guo, J. Gamelin, S. Yan, M.M. Sanders, M. Brewer, Q. Zhu, Coregistered three-dimensional ultrasound and photoacoustic imaging system for ovarian tissue characterization, J. Biomed. Opt. 14 (5) (2009) 054014.
[17] M. Jaeger, L. Siegenthaler, M. Kitz, M. Frenz, Reduction of background in optoacoustic image sequences obtained under tissue deformation, J. Biomed. Opt. 14 (5) (2009) 054011.
[18] K. Daoudi, P.J. van den Berg, O. Rabot, A. Kohl, S. Tisserand, P. Brands, W. Steenbergen, Handheld probe integrating laser diode and ultrasound transducer array for ultrasound/photoacoustic dual modality imaging, Opt. Express 22 (21) (2014) 26365–26374.
[19] J.C. Bamber, Acoustical characteristics of biological media, in: M.J. Crocker (Ed.), Encyclopedia of Acoustics, John Wiley & Sons, IncHoboken, NJ, USA, 2007, pp. 1703–1726.
[20] T.D. Khokhlova, I.M. Pelivanov, V.V. Kozhushko, A.N. Zharinov, V.S. Solomatin, A.A. Karabutov, Optoacoustic imaging of absorbing objects in a turbid medium: ultimate sensitivity and application to breast cancer diagnostics, Appl. Opt. 46 (2) (2007) 262–272.
[21] M. Frenz, M. Jaeger, Optimization of Tissue Irradiation in Optoacoustic Imaging Using a Linear Transducer: Theory and Experiments, SPIE BiOS, SPIE, 2008 (p. 13).
[22] G. Held, S. Preisser, H.G. Akarcay, S. Peeters, M. Frenz, M. Jaeger, Effect of irradiation distance on image contrast in epi-optoacoustic imaging of human volunteers, Biomed. Opt. Express 5 (11) (2014) 3765–3780.
[23] S. Preisser, G. Held, H.G. Akarcay, M. Jaeger, M. Frenz, Study of clutter origin in-vivo epi-optoacoustic imaging of human forearms, J. Optics-Uk 18 (9) (2016) 094003.
[24] X.D. Wang, G. Ku, M.A. Wegiel, D.J. Bornhop, G. Stoica, L.H.V. Wang, Noninvasive photoacoustic angiography of animal brains in vivo with near-infrared light and an optical contrast agent, Opt. Lett. 29 (7) (2004) 730–732.
[25] D. Wu, L. Huang, M.S. Jiang, H.B. Jiang, Contrast agents for photoacoustic and thermoacoustic imaging: a review, Int. J. Mol. Sci. 15 (12) (2014) 23616–23639.
[26] X.L. Dean-Ben, S. Gottschalk, B. Mc Larney, S. Shoham, D. Razansky, Advanced optoacoustic methods for multiscale imaging of in vivo dynamics, Chem. Soc. Rev. 46 (8) (2017) 2158–2198.
[27] S. Lin, A. Shah, J. Hernandez-Gil, A. Stanziola, B.I. Harriss, T.O. Matsunaga, N. Long, J. Bamber, M.X. Tang, Optically and acoustically triggerable sub-micron phase-change contrast agents for enhanced photoacoustic and ultrasound imaging, Photoacoustics 6 (2017) 26–36.
[28] K.E. Wilson, S.V. Bachawal, L. Abou-Elkacem, K. Jensen, S. Machtaler, L. Tian, J.K. Willmann, Spectroscopic photoacoustic molecular imaging of breast cancer using a B7-H3-targeted ICG contrast agent, Theranostics 7 (6) (2017) 1463–1476.
[29] M. Jaeger, S. Preisser, M. Kitz, D. Ferrara, S. Senegas, D. Schweizer, M. Frenz, Improved contrast deep optoacoustic imaging using displacement-compensated averaging: breast tumour phantom studies, Phys. Med. Biol. 56 (18) (2011) 5889–5901.
[30] M. Jaeger, D. Harris-Birtill, A. Gertsch, E. O'Flynn, J. Bamber, Deformation-compensated averaging for clutter reduction in epiphotoacoustic imaging in vivo, J. Biomed. Opt. 17 (6) (2012) 066007.
[31] M. Jaeger, K. Gashi, H.G. Akarçay, G. Held, S. Peeters, T. Petrosyan, S. Preisser, M. Gruenig, M. Frenz, Real-time clinical clutter reduction in combined epi-optoacoustic and ultrasound imaging, Photonics Lasers Med. 3 (4) (2014) 343–349.
[32] M.K.A. Singh, W. Steenbergen, Photoacoustic-guided focused ultrasound (PAFUSion) for identifying reflection artifacts in photoacoustic imaging, Photoacoustics 3 (4) (2015) 123–131.
[33] M.K.A. Singh, M. Jaeger, M. Frenz, W. Steenbergen, In vivo demonstration of reflection artifact reduction in photoacoustic imaging using synthetic aperture photoacoustic-guided focused ultrasound (PAFUSion), Biomed. Opt. Express 7 (8) (2016) 2955–2972.
[34] H.M. Schwab, M.F. Beckmann, G. Schmitz, Photoacoustic clutter reduction by inversion of a linear scatter model using plane wave ultrasound measurements, Biomed. Opt. Express 7 (4) (2016) 1468–1478.
[35] H.-M. Schwab, G. Schmitz, An advanced interpolation approach for photoacoustic clutter reduction based on a linear plane wave scatter model, Ultrasonics Symposium (IUS) 2016 IEEE Int. IEEE (2016) 1–4.
[36] E.J. Alles, M. Jaeger, J.C. Bamber, Photoacoustic clutter reduction using short-lag spatial coherence weighted imaging, Ultrasonics Symposium (IUS) 2014 IEEE Int. IEEE (2014) 41–44.
[37] M.A.L. Bell, R. Goswami, J.A. Kisslo, J.J. Dahl, G.E. Trahey, Short-lag spatial coherence imaging of cardiac ultrasound data: initial clinical results, Ultrasound Med. Biol. 39 (10) (2013) 1861–1874.
[38] M. Jaeger, J.C. Bamber, M. Frenz, Clutter elimination for deep clinical optoacoustic imaging using localised vibration tagging (LOVIT), Photoacoustics 1 (2) (2013) 19–29.
[39] M. Theodorou, M. Jaeger, J. Fromageau, T. Petrosyan, M.-X. Tang, M. Frenz, J. Bamber, Single transducer LOVIT-enabled photoacoustic imaging: a feasibility study, ultrasonics symposium (IUS), IEEE Int. IEEE 2016 (2016) 1–4.
[40] A.A. Oraevsky, A.A. Karabutov, S.V. Solomatin, E.V. Savateeva, V.G. Andreev, Z. Gatalica, H. Singh, R.D. Fleming, Laser optoacoustic imaging of breast cancer in vivo, Biomed. Optoacoust. Ii 4256 (2001) 6–15.
[41] M. Pramanik, G. Ku, C.H. Li, L.V. Wang, Design and evaluation of a novel breast cancer detection system combining both thermoacoustic (TA) and photoacoustic (PA) tomography, Med. Phys. 35 (6) (2008) 2218–2223.
[42] G.R. Torr, The acoustic radiation force, Am. J. Phys. 52 (5) (1984) 402–408.
[43] J. Bercoff, M. Tanter, M. Fink, Supersonic shear imaging: a new technique for soft tissue elasticity mapping, IEEE Trans. Ultrason Ferroelectr. 51 (4) (2004) 396–409.
[44] K. Nightingale, M.S. Soo, R. Nightingale, G. Trahey, Acoustic radiation force impulse imaging: in vivo demonstration of clinical feasibility, Ultrasound Med. Biol. 28 (2) (2002) 227–235.
[45] D. Melodelima, J.C. Bamber, F.A. Duck, J.A. Shipley, L.J. Xu, Elastography for breast cancer diagnosis using radiation force: system development and performance evaluation, Ultrasound Med. Biol. 32 (3) (2006) 387–396.
[46] D. Melodelima, J.C. Bamber, F.A. Duck, J.A. Shipley, Transient elastography using impulsive ultrasound radiation force: a preliminary comparison with surface palpation elastography, Ultrasound Med. Biol. 33 (6) (2007) 959–969.
[47] B.J. Tromberg, O. Coquoz, J. Fishkin, T. Pham, E.R. Anderson, J. Butler, M. Cahn, J. D. Gross, V. Venugopalan, D. Pham, Non-invasive measurements of breast tissue optical properties using frequency-domain photon migration, Philos. Trans. R. Soc. B 352 (1354) (1997) 661–668.
[48] T. Durduran, R. Choe, J.P. Culver, L. Zubkov, M.J. Holboke, J. Giammarco, B. Chance, A.G. Yodh, Bulk optical properties of healthy female breast tissue, Phys. Med. Biol. 47 (16) (2002) 2847–2861.
[49] A.P. Sarvazyan, O.V. Rudenko, S.D. Swanson, J.B. Fowlkes, S.Y. Emelianov, Shear wave elasticity imaging: a new ultrasonic technology of medical diagnostics, Ultrasound Med. Biol. 24 (9) (1998) 1419–1435.
[50] R.G. Barr, Z. Zhang, Effects of precompression on elasticity imaging of the Breast development of a clinically useful semiquantitative method of precompression assessment, J. Ultrasound Med. 31 (6) (2012) 895–902.
[51] J. Lorenzen, R. Sinkus, G. Adam, Elastography Quantitative imaging modality of the elastic tissue properties, Rofo-Fortschr Rontg 175 (5) (2003) 623–630.
[52] W. Weiwad, A. Heinig, L. Goetz, H. Hartmann, D. Lampe, J. Buchmann, R. Millner, R.P. Spielmann, S.H. Heywang-Koebrunner, Direct measurement of sound velocity in various specimens of breast tissue, Invest. Radiol. 35 (12) (2000) 721–726.

[53] P.C. Beard, Photoacoustic imaging of blood vessel equivalent phantoms, Biomed. Optoacoust. Iii 4618 (2002) 54–62.
[54] S. Preisser, N.L. Bush, A.G. Gertsch-Grover, S. Peeters, A.E. Bailey, J.C. Bamber, M. Frenz, M. Jaeger, Vessel orientation-dependent sensitivity of optoacoustic imaging using a linear array transducer, J. Biomed. Opt. 18 (2) (2013) 026011.
[55] H.G. Nasief, I.M. Rosado-Mendez, J.A. Zagzebski, T.J. Hall, Acoustic properties of Breast fat, J. Ultrasound Med. 34 (11) (2015) 2007–2016.
[56] J. Ophir, N.F. Maklad, R.H. Bigelow, Ultrasonic-attenuation measurements of invivo human-Muscle, Ultrason. Imaging 4 (3) (1982) 290–295.
[57] T. Deffieux, G. Montaldo, M. Tanter, M. Fink, Shear wave spectroscopy for In vivo quantification of human soft tissues visco-elasticity, IEEE Trans. Med. Imaging 28 (3) (2009) 313–322.

**Tigran Petrosyan** received his Bachelor's degree in Physics from Yerevan State University, Armenia, in 2010, and Master's degree in Physics from ETH Zurich, Switzerland, in 2013. Currently, he is pursuing his PhD degree in Physics at the Biomedical Photonics group, University of Bern, Switzerland. His research specializes in optoacoustic imaging with focus on clutter reduction towards hand-held clinical applications.

**Maria Theodorou** received her MSc in Biomedical Engineering from Imperial College London in 2010. After working in the private sector the following two years, she joined the doctoral programme of the Institute of Cancer Research, University of London. She recently completed her PhD in Medical Physics funded by Cancer Research UK, and is currently a postdoctoral researcher at the Institute of Cancer Research and Royal Marsden Hospital, working in the area of quantitative ultrasound imaging and elastography methods.

**Jeff Bamber** is Professor in Physics Applied to Medicine, leader of the Ultrasound and Optical Imaging Team and a Senior Tutor at the Institute of Cancer Research London. He holds honorary appointments at the Royal Marsden and other hospitals and colleges in London. He has contributed to subjects such as understanding the acoustic characteristics of normal and malignant tissues, ultrasound image formation, speckle and clutter reduction, elastography and photoacoustic imaging. His current research aims to increase ultrasound functional and molecular imaging capability, providing tools to experimental cancer biology and helping to improve cancer treatment by bringing ultrasound-based methods to clinical problems such as early diagnosis, assessing tumour aggressiveness and response, and guiding treatment. He is past president of the International Association for Breast Ultrasound and past vice-president of the International Society of Skin Imaging.

**Martin Frenz** received the Dipl Phys degree in physics from the Albert-Ludwig University of Freiburg, Germany, in 1985, and the PhD in physics from the University of Bern, Switzerland in 1990. In 1995 he joined the University of Texas at Austin, USA. In 2002 he became a professor and head of the biomedical photonics department of the Institute of Applied Physics at the University of Bern, Switzerland. Since 2008 he is director of the Institute of Applied Physics. His current research focuses on optoacoustic sensing and imaging, biomedical applications of lasers and optical diagnostics.

**Michael Jaeger** received the Dipl Phil Nat degree in physics from the University of Bern, Switzerland, in 2002, and the PhD in physics from the same university in 2007. In 2010/2011 he joined the Institute of Cancer Research and the Royal Marsden Hospital, Sutton, UK. In 2012 he won a grant for a three-year project under the career development scheme “Ambizione” from the Swiss National Science Foundation, and is now group leader of the Optoacoustic Imaging Team at the Institute of Applied Physics, University of Bern. His research includes optoacoustic imaging with focus on clinical imaging, as well as novel ultrasound imaging methods.